Nano Research 2018, 11(5): 2436–2449
https://doi.org/10.1007/s12274-017-1865-z
Research Article
ISSN 1998-0124
CN 11-5974/O4

Polyethylene glycol-modified cobalt sulfide nanosheets for high-performance photothermal conversion and photoacoustic/magnetic resonance imaging

Zhenglin Li[1,2,3], Zhuo Li[1], Lei Chen[4], Ying Hu[5], Shaoshan Hu[4], Zhaohua Miao[6], Ye Sun[2] (✉), Flemming Besenbacher[3] (✉), and Miao Yu[1] (✉)

[1] *State Key Laboratory of Urban Water Resource and Environment, School of Chemical Engineering and Technology, Harbin Institute of Technology, Harbin 150001, China*
[2] *Condensed Matter Science and Technology Institute, Harbin Institute of Technology, Harbin 150001, China*
[3] *Interdisciplinary Nanoscience Center (iNANO) and Department of Physics and Astronomy, Aarhus University, Aarhus 8000, Denmark*
[4] *Department of Neurological Surgery, The Second Affiliated Hospital of the Harbin Medical University, Harbin 150001, China*
[5] *School of Life Science and Technology, Harbin Institute of Technology, Harbin 150001, China*
[6] *School of Materials Science and Engineering, Harbin Institute of Technology, Harbin 150001, China*

Received: 12 June 2017
Revised: 21 September 2017
Accepted: 23 September 2017

KEYWORDS

cobalt sulfide nanosheets, theranostic agent, photoacoustic imaging, magnetic resonance imaging, photothermal therapy

ABSTRACT

Theranostic nanoagents that integrate the diagnoses and therapies within a single nanomaterial are compelling in their use for highly precise and efficient antitumor treatments. Herein, polyethylene glycol (PEG)-modified cobalt sulfide nanosheets (CoS-PEG NSs) are synthesized and unitized as a powerful theranostic nanoagent for efficient photothermal conversion and multimodal imaging for the first time. We demonstrate that the obtained CoS-PEG NSs show excellent compatibility and stability in water and various physiological solutions, and can be effectively internalized by cells, but exhibit a low cytotoxicity. The CoS-PEG NSs exhibit an efficient photothermal conversion capacity, benefited from the strong near-infrared (NIR) absorption, high photothermal conversion efficiency (~ 33.0%), and excellent photothermal stability. Importantly, the highly effective photothermal killing effect on cancer cells after exposure to CoS-PEG NSs plus laser irradiation has been confirmed by both the standard Cell Counting Kit-8 and live-dead cell staining assays, revealing a concentration-dependent photothermal therapeutic effect. Moreover, utilizing the strong NIR absorbance together with the T_2-MR contrast ability of the CoS-PEG NSs, a high-contrast triple-modal imaging, i.e., photoacoustic (PA), infrared thermal (IRT), and magnetic resonance (MR) imaging, can be achieved, suggesting a great potential for multimodal imaging to provide comprehensive cancer diagnosis. Our work introduces the first bioapplication of the CoS-PEG nanomaterial as a potential theranostic nanoplatform and may promote further rational design of CoS-based nanostructures for precise/efficient cancer diagnosis and therapy.

Address correspondence to Miao Yu, miaoyu_che@hit.edu.cn; Ye Sun, sunye@hit.edu.cn; Flemming Besenbacher, fbe@inano.au.dk

1 Introduction

The development of safe and effective antitumor techniques is in great demand, as cancer remains one of the most serious threats to human health [1, 2]. One of the most promising alternatives or supplements to traditional cancer therapy (surgery, radiotherapy, and chemotherapy), is photothermal therapy (PTT). Many advantages of PTT, based on the interaction between tumors and tissue-transparent near-infrared (NIR, λ = 700–1,100 nm) light irradiation, have been demonstrated, such as operational simplicity, high efficiency, and minimal invasiveness [3–5]. The photothermal therapeutic effect is highly dependent on the properties of the photothermal agents (PTAs) [6]. Hitherto, diverse types of PTAs have been successfully fabricated, including noble metallic nanostructures (e.g., gold nanorods, gold nanoshells, and Pd nanosheets), inorganic semiconductor nanoparticles (e.g., Bi_2Se_3, Bi_2S_3, CuS, WS_2, MoS_2, and Prussian blue) and carbon nanomaterials (e.g., carbon nanotubes and graphene oxide), that have produced extraordinary results for *in vivo*/*in vitro* antitumor PTT treatments [7–14]. However, certain inherent defects of the developed PTAs, such as high costs, complicated syntheses, insufficient photothermal conversion efficiency, poor photothermal stability, and relatively low *in vivo* biocompatibility, have promoted great interest in new high performance PTAs [15, 16].

Besides the therapeutic efficacy, the accurate and timely diagnosis is also pivotal in clinical antitumor treatments. Evidently, separate conventional agents for diagnosis or therapies inevitably often cause poor bioavailability, impaired target specificity, and superfluous metabolic burden [17]. Recent advances in nanotechnology have offered brilliant solutions to address these issues, i.e., theranostics [19] that combines multi-modal diagnostic and therapeutic moieties within a single nanoplatform [18]. In most cases, due to a lack of requisite imaging functions, PTAs always require further modification or functionalization to integrate multiple imaging modes (e.g., magnetic resonance imaging (MRI), computed tomography (CT), or fluorescence (FL) imaging) to precisely and sensitively provide *in situ* diagnostic information regarding the tumor spatial location, size and the agent's accumulation at the target site, and to monitor the treatment progress and evaluate the efficacy after PTT [10, 20, 21].

Among all the clinically available imaging modalities, MRI has drawn considerable attention as it can provide exquisite three-dimensional (3D) soft-tissue anatomical details and functional information with high spatial and temporal resolution as well as unlimited tissue penetration [22]. Moreover, studies also show that MRI can monitor real-time temperature changes in tumor tissues, providing useful feedback information for the PTT procedure [23]. Therefore, integrating MRI and PTT functions into a single nanoagent (namely magnetic PTAs) is compelling for their use in highly precise and efficient imaging-guided cancer therapy. To date, several kinds of magnetic PTAs have been fabricated by combining one agent for the PTT with a second component for the MRI, e.g., Fe_3O_4@Cu_{2-x}, Fe_3O_4@Prussian blue, and MnSe@Bi_2Se_3 core–shell nanostructures [24–26]. In these cases, complex compositions, cumbersome synthetic processes, and overmuch material costs are demanded. Moreover, such complex modular-combined architectures still suffer from the inconsonant module doses required for imaging/therapy together with the complicated degradation and excretion behaviors of different functional components during circulation/metabolism *in vivo*, resulting in discrepant pharmacokinetics and unsatisfactory therapeutic performances [27–29]. Therefore, it is highly desirable but challenging to develop single-component high-performance magnetic PTAs with low toxicity for clinical applications.

Recently, due to the strong NIR absorption and unpaired 3d electrons [30], cobalt-based binary/ternary bimetal chalcogenide nanomaterials, such as Co_9Se_8 nanoplates and $CuCo_2S_4$ nanocrystals, have been developed as single-component magnetic PTAs for multimodal imaging-guided PTT [27, 31, 32]. Albeit these inspiring results, the reported Co-based nanoagents are still scarce and some intrinsic defects, such as complicated synthesis, lack of proper surface modification, and the excess metabolic burden of additional Cu elements, hamper their clinical applications. Consequently, we aim to explore other Co chalcogenides based nanostructures via a facile synthesis approach to extend their application for cancer diagnosis and therapy.

Herein, we have developed, for the first time in the literature, a novel theranostic nanoplatform based on CoS nanoplates for efficient photothermal conversion and MR/photoacoustic (PA)/infrared thermal (IRT) triple-modal imaging (Scheme 1). The CoS nanoplates are synthesized via a simple one-step hydrothermal process under an alkaline condition and coated with polyvinylpyrrolidone (PVP); a well-demonstrated biocompatible and biodegradable polymer stabilizer commonly-used in the biomedicine field. After further surface functionalization with polyethylene glycol (PEG, $M_W \approx 2{,}000$), the obtained CoS-PEG NSs showed excellent compatibility and stability in water and various physiological solutions, that are the prerequisites for clinical application. We demonstrate that the PEGylated CoS NSs can be effectively internalized by cells with low cytotoxicity. Importantly, the CoS-PEG NSs exhibited strong NIR photo-absorption, a high photothermal conversion efficiency (~ 33.0%), and an excellent photothermal conversion stability. When simultaneously treated with the CoS-PEG NSs and NIR laser irradiation, cancer cells can be killed efficiently and the significant photothermal ablation effects are enhanced rapidly with increased concentrations. Moreover, derived from the strong NIR absorbance as well as the T_2-MR contrasting ability of the CoS-PEG NSs, high-contrast PA, IRT, and MR imaging has been achieved, showing great potential for multimodal imaging in providing comprehensive cancer diagnoses.

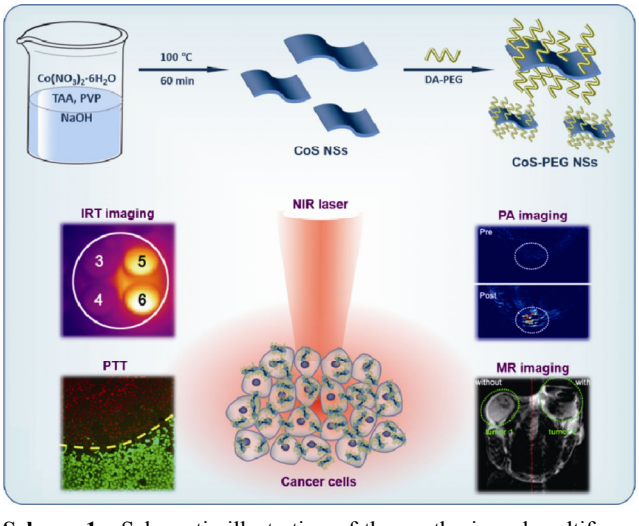

Scheme 1 Schematic illustration of the synthesis and multifunction of the CoS-PEG NSs.

Our results imply great potential of CoS-PEG NSs as a safe and powerful theranostic nanoplatform for triple-modal imaging and PTT applications.

2 Experimental

2.1 Materials

$Co(NO_3)_2 \cdot 6H_2O$ (≥ 99%), thioacetamide (TAA, ≥ 99%), NaOH (≥ 97%) and absolute ethanol (≥ 99.8%, GR) were obtained from Aladdin (China). Polyvinylpyrrolidone (PVP, $M_W \approx 55{,}000$) was ordered from Sigma-Aldrich (USA). Dopamine-modified polyethylene glycol (DA-PEG, $M_W \approx 2{,}000$) was provided by Xi'an Ruixi Biological Technology Co., Ltd. (China). The Cell Counting Kit-8 (CCK-8), calcein acetoxymethyl ester (Calcein AM, > 90%), and propidium iodide (PI) were purchased from Dojindo Laboratories. The cell-culture-related materials, such as Dulbecco's modified Eagle's medium (DMEM), fetal bovine serum (FBS), and phosphate buffer solution (PBS) were purchased from Gibco Co. (USA). All of the chemicals were of analytical grade and used as received from the manufacturers. Deionized (DI) water obtained from a Milli-Q water purification system (resistivity ~ 18.2 MΩ·cm) was used in all experiments.

2.2 Synthesis of CoS-PEG nanosheets (NSs)

CoS NSs were first synthesized according to the method in Ref. [33] with some modifications. Typically, $Co(NO_3)_2 \cdot 6H_2O$ (291 mg), TAA (150 mg), and PVP (200 mg) were dissolved in DI water (50.0 mL). Following the addition of NaOH aqueous solution (0.5 mol·L^{-1}, 12.0 mL) under magnetic stirring, the mixture solution was then heated and maintained at 100 ˚C for 60 min. During the reaction, the solution color changed from aquamarine to black, indicating the formation of the CoS NSs. After cooling to room temperature, the obtained product was centrifuged (10,000 rpm, 10 min) to collect the precipitate, and then thoroughly washed three times with DI water and three times with absolute ethanol. For the PEG coating, the as-prepared CoS NSs were re-dispersed in a DA-PEG aqueous solution (2.0 mg·mL^{-1}) and stirred overnight. Excess DA-PEG molecules were removed by centrifugation (10,000 rpm, 10 min) and

washed with DI water repeatedly, followed by freeze-drying for further use.

2.3 Materials characterization

The morphology of the CoS-PEG NSs was characterized by transmission electron microscopy (TEM, Tecnai G20, FEI Co., USA) at an acceleration voltage of 200 kV. The elemental composition of the sample was analyzed using energy dispersive spectroscopy (EDS, SU8020, Hitachi Limited, Japan). The dynamic light scattering (DLS) measurement was conducted by using a 90Plus/BI-MAS instrument (Brookhaven Instruments Co., USA). The optical absorption spectra of the CoS-PEG NSs were collected by an ultraviolet–visible–near-infrared spectrophotometer (UV–vis–NIR, Evolution 300, Thermo Scientific, USA). The Co element content in the sample solution was analyzed by inductively coupled plasma atomic emission spectroscopy (ICP-MS, Thermo Scientific, USA).

2.4 Photothermal effect measurement

To study the photothermal effect, 1.0 mL of the CoS-PEG NSs aqueous dispersions at different concentrations (0–200 $\mu g \cdot mL^{-1}$) were added into quartz cuvettes and then irradiated by a 808 nm laser (Beijing Kaipulin Optoelectronic Technology Co., China) at 1.2 $W \cdot cm^{-2}$ for 10 min. The solution temperature was recorded every 1 s by a thermocouple microprobe (Q50.5 mm, STPC-510P, Xiamen Baidewo Technology Co., China) with an accuracy of 0.1 ℃. For measuring the photothermal conversion efficiency (η), the CoS-PEG dispersion (200 $\mu g \cdot mL^{-1}$) was irradiated by the NIR laser until the system temperature reached a steady state. The laser was then turned off, and the temperature was allowed to cool to room temperature. Pure DI water was used as the control. To study the photothermal stability, the CoS-PEG dispersion (200 $\mu g \cdot mL^{-1}$) was repeatedly irradiated by the 808-nm laser for 7 cycles (3 min irradiation for each cycle). Then, the treated CoS-PEG after the repeated cycles was collected for the UV–vis–NIR absorption measurement.

2.5 Photothermal ablation on cancer cells

The localized photothermal effect of the CoS-PEG NSs was evaluated on murine breast cancer 4T1 cells, which were cultured in normal DMEM supplemented with 10% FBS and 1% penicillin/streptomycin at 37 ℃ in an atmosphere of 5% CO_2 and 95% air. For the qualitative analysis, 4T1 cells seeded onto a 24-well plate at a density of 5×10^5 cells per well were incubated with the CoS-PEG NSs dispersions (1.0 mL per well, 60 $\mu g \cdot mL^{-1}$), and then exposed to the 808-nm laser for 10 min. After irradiation, the cells were washed repeatedly with PBS, then stained with calcein-AM (2.0 $\mu mol \cdot L^{-1}$) and PI (3.0 $\mu mol \cdot L^{-1}$) for observation of the live and dead cells using an inverted fluorescence microscope (IX71, Olympus, Japan). To further study the cell viability upon irradiation, the CCK-8 assay was employed to evaluate the photothermal effect on the cancer cells. Typically, 4T1 cells seeded onto a 96-well plate (1×10^4 cells per well) were incubated with the CoS-PEG NSs dispersions of different concentrations (0–60 $\mu g \cdot mL^{-1}$), followed by irradiation with the 808-nm laser for 10 min. After irradiation, the cell viability was evaluated using the CCK-8 assay.

2.6 Cellular uptake of CoS-PEG NSs

4T1 cells seeded onto 6-well plates (1×10^6 cells per well) were incubated with the CoS-PEG NSs dispersions (20 and 50 $\mu g \cdot mL^{-1}$) for 3, 6, and 12 h, respectively. After incubation, the cells were washed three times with PBS to remove free NSs, then trypsinized and carefully collected by centrifugation (800 rpm, 5 min). After counting by a hemocytometer, the cells with a density of 1×10^6 cells were lysed in the strong oxidizing mixture, i.e., concentrated nitric acid and H_2O_2 (volume ratio = 5:1). After 24 h, the mixture was heated to 120 ℃ to evaporate all of the solvent, and sequentially cooled to room temperature. Diluted nitric acid (2%, 10 mL) was added to dissolve the remaining residues, and the obtained samples were finally analyzed using ICP-MS.

2.7 Cytotoxicity/hemolysis assay

To assess the potential cytotoxicity of the CoS-PEG NSs, 4T1 cells and human umbilical vein endothelial cells (HUVEC) seeded onto 96-well plates (1×10^4 cells per well) were incubated with the CoS-PEG NSs dispersions at selected concentrations (0–150 $\mu g \cdot mL^{-1}$)

for 24 h. The CCK-8 assay was used to measure the cell viability according to the manufacturer suggested procedures.

To study hemolysis, a blood sample (1.0 mL, stabilized by ethylenediamine tetraacetic acid) was collected from a Balb/C female mouse by removing the eye ball, and added into PBS (2.0 mL), followed by centrifugation (3,000 rpm, 10 min) to separate the red blood cells (RBCs) from serum. The obtained RBCs were further washed five times and diluted into PBS (10.0 mL). The diluted RBC suspension (200 μL) was then incubated with the CoS-PEG NSs dispersions of different concentrations (0–200 $\mu g \cdot mL^{-1}$, 800 μL) for 4 h at room temperature. Afterwards, the samples were centrifugated (10,000 $rpm \cdot min^{-1}$, 10 min) to collect the supernatant for UV–vis absorbance (577 nm) measurement. The DI water and PBS were used as the positive and negative control groups, respectively.

2.8 *In vitro/in vivo* PA imaging and MRI

The *in vitro* PA effect was studied by loading the CoS-PEG NSs suspensions of different concentrations (0–320 $\mu g \cdot mL^{-1}$) into agar gel cylinders with a diameter ~ 1.0 cm, and then placed in an MSOT InVision 128 PA tomography system (iThera Medical, Germany) for PA scanning. The corresponding average PA signal of each sample was calculated from the region of interest after image reconstruction. To investigate the PA imaging effect *in vivo*, the CoS-PEG NSs suspension (1.0 $mg \cdot mL^{-1}$, 100 μL) was intratumorally (i.t.) injected into the tumor-bearing mice for PA scanning. PA images of the mice before the injection were also collected as the control. All of the animal involved experiments were performed according to protocols approved by the Institutional Animal Care and Use Committee.

To measure the T_2-weighed relaxation property *in vitro*, the CoS-PEG NSs aqueous dispersions with gradient Co concentrations (i.e., 0, 0.06, 0.12, 0.24, 0.40, and 0.75 $mmol \cdot L^{-1}$) were scanned by Siemens Prisma 3.0 T MR scanner (Erlangen, Germany) with a gradient strength of up to 80 $mT \cdot m^{-1}$. The relaxation rate r_2 ($(mM)^{-1} \cdot s^{-1}$) was calculated from the linear-fitting slope of $1/T_2$ values (s^{-1}) as a function of Co concentrations. The T_2-MR contrast enhancement effect on the 4T1 cells was also investigated as follows: 4T1 cells seeded in 6-well plates (5×10^5 cells per well) were incubated with the CoS-PEG NSs dispersions (concentration of 0, 75, and 150 $\mu g \cdot mL^{-1}$) for 12 h, then harvested, washed three times and finally dispersed in PBS (1.0 mL) for MRI scanning. For *in vivo* MRI, the CoS-PEG NSs dispersion was i.t. injected into one of the tumors of the double-tumor-bearing mouse and then the mouse was anesthetized for MRI scanning. Cross-sectional and coronal two-dimensional (2D) turbo spin echo T_2-weighted images were acquired with the following parameters: TR = 6,140 ms and TE = 88 ms.

3 Results and discussion

3.1 Synthesis and characterization

The CoS NSs were first synthesized through a simple one-step hydrothermal process under an alkaline condition at 100 °C and stabilized with PVP ($M_W \approx$ 55,000), providing the NSs high water solubility. The alkaline condition played an important role in the NSs formation, since no CoS NSs product could be obtained in the absence of NaOH. In the presence of PVP, the alkaline environment allowed Co^{2+} to react with OH^- to obtain PVP-stable hexagonal β-$Co(OH)_2$ (aquamarine) in the aqueous solution. After heating to 100 °C, the TAA underwent thermal decomposition, generating S^{2-} ions before reacting with the as-prepared $Co(OH)_2$ precursors forming the CoS NSs (black). The formation mechanism is based on the following reactions

$$Co^{2+} + 2OH^- \rightarrow Co(OH)_2 \quad (1)$$

$$Co(OH)_2 + S^{2-} \rightarrow CoS + 2OH^- \quad (2)$$

TEM and AFM were employed to characterize the morphology of the obtained CoS sample. The typical TEM images (Fig. 1(a) and Fig. S1 in the Electronic Supplementary Material (ESM)) and the statistical analysis of the size distribution (Fig. 1(b)) showed that the average lateral diameter of the obtained particles was ~ 179 nm (with the size ranging from ~ 102 to ~ 275 nm). The AFM results (Figs. 1(c) and 1(d)) further revealed that the average thickness of the individual particles was ~ 7 nm, indicating their distinct

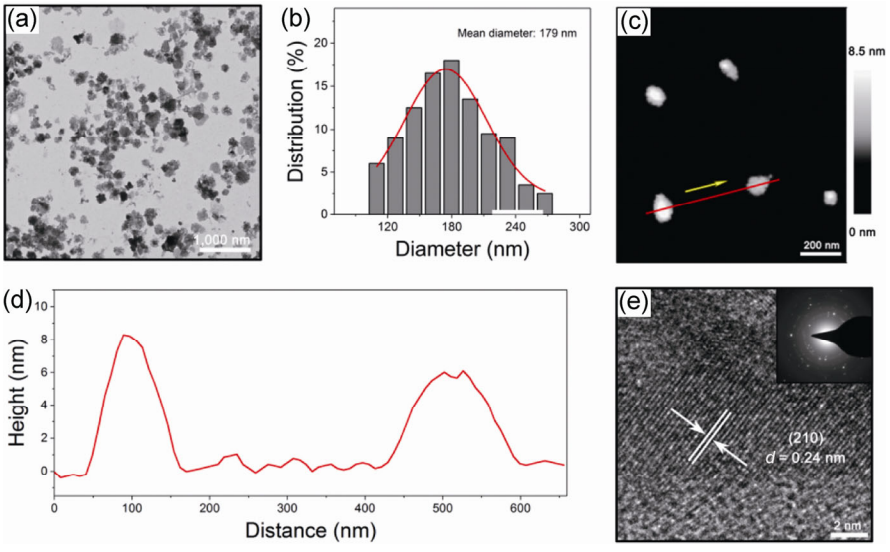

Figure 1 (a) TEM image, (b) corresponding diameter distribution histogram (n = 200), and (c) AFM image of the synthesized CoS NSs. (d) The corresponding height graph of two random CoS NSs shown in (c). (e) HRTEM (inset: the SAED pattern) images of the CoS NSs.

nanosheet morphology. The DLS measurement confirmed that the average hydrodynamic size of the NSs was ~ 184 nm, in good agreement with the TEM results. The high-resolution TEM (HRTEM) image (Fig. 1(e)) shows a hexagonal crystal lattice with a lattice spacing of ~ 0.24 nm, corresponding to the spacing of the CoS (210) crystal planes. Moreover, the element mapping images of a single CoS NS via high-angle annular detector dark-field scanning transmission electron microscopy (HAADF-STEM) suggested homogeneous distributions of Co (green) and S (red) elements in the NSs (Fig. 2(a)). The EDS analysis further confirmed the chemical composition of the CoS NSs and revealed that the elemental atom ratio of Co:S was ~ 0.99:1 (Fig. 2(b)). Note that the light element C and O peaks in the spectrum were attributed to the PVP polymer stabilizer and the carbon-coated sample substrate for the measurement.

In order to improve the compatibility and stability of the CoS NSs in physiological solutions, which is the prerequisite for practical application in biological systems, we then functionalized the surface of the NSs with PEG (Scheme 1). The obtained CoS-PEG NSs aqueous dispersion was a transparent black color, implying their good dispersity in water. Furthermore, the CoS-PEG NSs showed slightly increased hydrodynamic sizes (~ 196 nm) together with a low polydispersity index (PDI ~ 0.190) as measured by DLS, further demonstrating the high dispersity. Moreover, the CoS-PEG NSs showed excellent compatibility

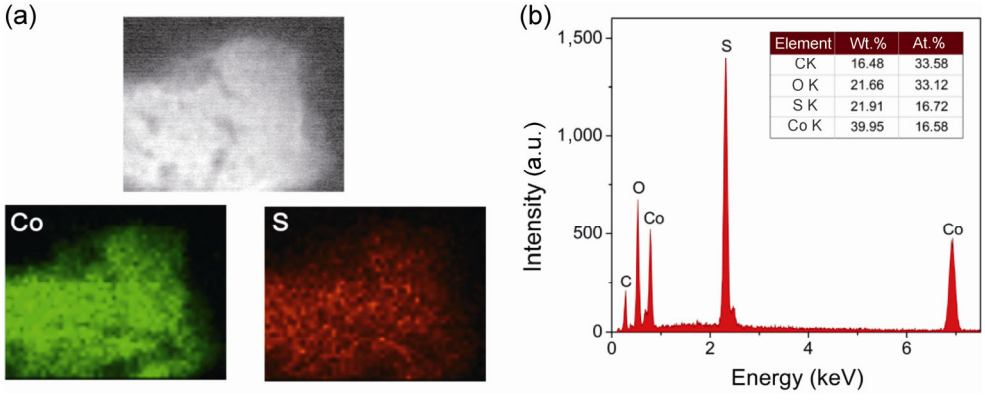

Figure 2 (a) HAADF-STEM image and the corresponding element mapping of an individual CoS NS, showing the elemental distribution of Co (green) and S (red). (b) EDS analysis of CoS NSs.

and stability in DI water and various physiological solutions, such as PBS, DMEM cell medium, and FBS without macroscopic aggregation for long-time storage (Fig. S2 in the ESM). The high stability was further confirmed by the perfect linearly increased absorbance with increased NSs concentrations in both water and the DMEM medium (Fig. S3 in the ESM). In addition, the Co ion leakage experiment showed almost no Co ions were released from the NSs after 7-days of dialysis (Fig. S4 in the ESM).

3.2 Photothermal properties

Strong NIR optical absorbance and high photothermal conversion efficiency are essential for competent PTAs [12]. It has been demonstrated that nanomaterials with a thin-flake shape can benefit from both their light absorbance and photothermal effects [34]. The UV–vis–NIR absorption spectrum of the CoS-PEG NSs was measured to investigate their optical properties. As shown in Fig. 3(a), the CoS-PEG NSs exhibited significant and broad absorption in the NIR region (from 700 to 900 nm), showing great promise for NIR irradiation-driven PTT. We then evaluated the photothermal effect of the CoS-PEG NSs by measuring the temperature of the NSs aqueous dispersion at gradient concentrations upon irradiation by the optical fiber coupled 808-nm laser (1.2 W·cm^{-2}). We chose the 808-nm irradiation because of its large absorption coefficient and deep tissue penetration. Clearly, the CoS-PEG NSs exhibited a significant concentration-dependent photothermal effect (Fig. 3(b)). When the concentrations of the CoS-PEG NSs dispersions gradually increased from 10 to 200 μg·mL^{-1}, the temperature elevation (ΔT) was enhanced from 5.3, to 9.7, 16.3, 26.8, and 36.4 ˚C with 10-min of irradiation (Fig. S5 in the ESM). In sharp contrast, the temperature rise of pure DI water with the same irradiation treatment was negligible (~ 1.9 ˚C). It should be emphasized that at 200 μg·mL^{-1} the NSs dispersion temperature increased to 67.2 ˚C after 10-min of irradiation. Moreover, after a short irradiation, less than 1.5 min, the temperature reached the critical

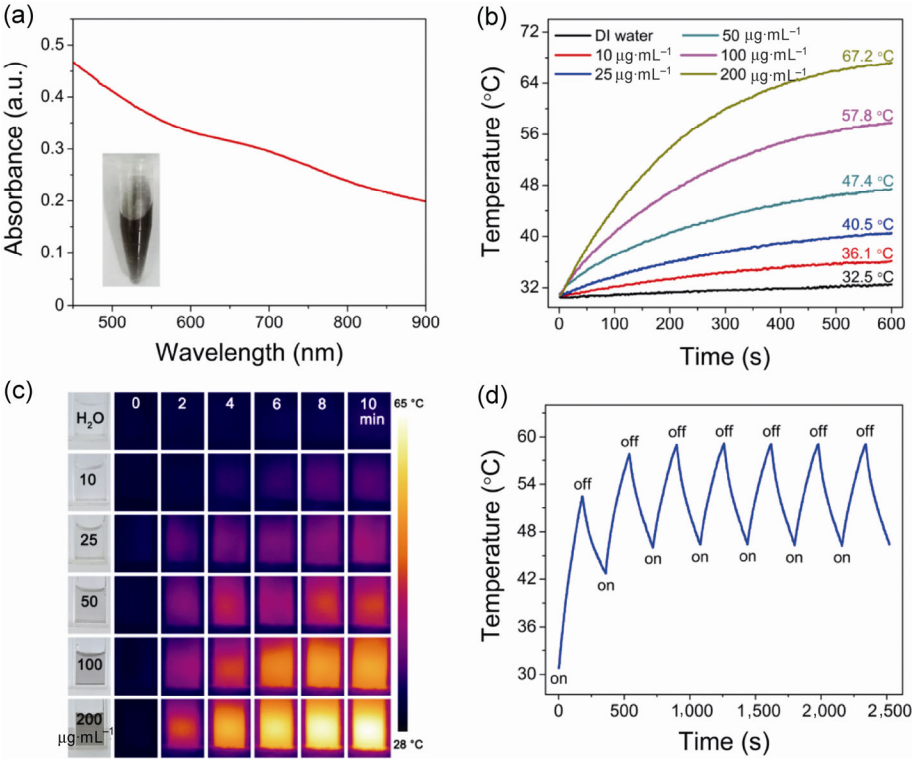

Figure 3 (a) UV–vis–NIR absorption spectrum of the CoS-PEG NSs dispersed in DI water (Inset: Photo of the CoS-PEG aqueous suspension). (b) Temperature elevation and (c) IR thermal images of the CoS-PEG NSs suspensions at various concentrations (0–200 μg·mL^{-1}) with 10-min of irradiation. (d) Temperature elevation of the CoS-PEG NSs suspension (200 μg·mL^{-1}) over 7 repeated irradiation cycles (3-min irradiation for each cycle).

temperature (~ 43 ℃), inducing the apoptosis of cancer cells [35]. Such strong photothermal effects of CoS-PEG NSs were also used for high-contrast IRT imaging, where the intensity relied on the concentration and the irradiation duration (Fig. 3(c)). It is well known that such an imaging mode is capable of providing added benefit to the real-time monitoring of the PTT treatment [24]. Moreover, as the photothermal stability of PTAs is also crucial for the PTT performance, we then explored the temperature rise of the NSs dispersion upon repeated laser "on-off" cycles. For each cycle, the dispersion was irradiated using the 808-nm laser for 3 min, followed by 3-min cooling (Fig. 3(d)). The CoS-PEG NSs was able to maintain the high temperature elevation during the cycles. Together with the unchanged absorption spectrum (Fig. S6 in the ESM) after the 7-cycle irradiation, it was clear that the CoS-PEG NSs possessed a high photothermal stability.

The photothermal conversion efficiency (η) is a pivotal factor in evaluating the photothermal capability of PTAs. To measure the photothermal conversion efficiency of the CoS-PEG NSs ($\eta_{\text{CoS-PEG}}$), the NSs aqueous dispersion (200 μg·mL^{-1}, 1.0 mL) was irradiated by the 808-nm laser to reach the maximum temperature, followed by natural cooling to room temperature. Based on Roper's report [36], $\eta_{\text{CoS-PEG}}$ can be calculated via Eq. (1)

$$\eta_{\text{CoS-PEG}} = \frac{hA(T_{\text{m}} - T_0) - Q_0}{I(1-10^{-A_{808}})} \quad (1)$$

where h is the heat transfer coefficient, A is the quartz cuvette surface area, T_{m} is the maximum temperature, and T_0 is the initial temperature. In our test (Fig. 4(a)), $\Delta T_{\text{max}} = (T_{\text{m}} - T_0)$ was ~ 40.5 ℃. Q_0 is the input baseline heat due to the light absorption by DI water and quartz cuvette, that is calculated by measuring the temperature elevation of pure water without the CoS-PEG NSs under the same conditions. I is the 808-nm laser power, A_{808} is the 808-nm absorbance of the CoS-PEG NSs dispersion. The value of hA can be obtained by linearly fitting the time data versus $-\ln(\Delta T/\Delta T_{\text{max}})$ in the cooling period (Fig. 4(b)), and calculated with Eq. (2)

$$\tau_{\text{s}} = \frac{\Sigma_i m_i C_{\text{p},i}}{hA} \quad (2)$$

where τ_{s} refers to the system thermal time constant, m_i is the mass, and $C_{\text{p},i}$ is the heat capacity. For our system, m = 1.0 g, C_{p} = 4.2 J·(g·℃)$^{-1}$, and τ_{s} = 370.0 s (Fig. 4(b)), and therefore hA is 11.4 mW·℃$^{-1}$. Substituting the hA value into Eq. (1), $\eta_{\text{CoS-PEG}}$ is calculated as ~ 33.0%, that is a much higher value than that of the widely-used Au nanomaterials (nanorods ~ 21% and nanoshells ~ 13%) [37]. Therefore, the strong NIR absorbance, high photothermal conversion efficiency and stability, as well as the commendable IRT imaging performance are advantageous for the CoS-PEG NSs as a promising PTT nanoagent.

3.3 Cellular uptake and cytotoxicity

Prior to studying the PTT efficacy on cancer cells, we

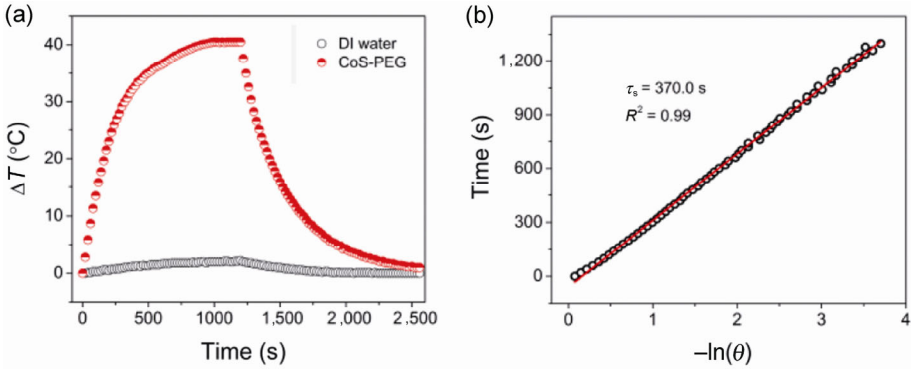

Figure 4 (a) Photothermal heating and cooling curves of the CoS-PEG NSs suspension (200 μg·mL^{-1}) and DI water (the control group) under 20-min laser irradiation, followed by switching of the laser. The CoS-PEG NSs suspension can achieve a maximum temperature rise of ~ 40.5 ℃, much higher than that of DI water (~ 2.2 ℃). (b) Linear time data versus −ln(θ) (the negative natural logarithm of the temperature driving force), obtained from the cooling period in Fig. 3(a).

first assessed the cellular uptake capability and biocompatibility of the CoS-PEG NSs *in vitro*. For the cellular-uptake study, 4T1 cells were incubated with the CoS-PEG NSs dispersions (20 and 50 μg·mL^{-1}) for different durations (3, 6, and 12 h), then collected and lysed for ICP-MS analysis to measure the Co element content. As shown in Fig. 5(a), the CoS-PEG NSs can be efficiently taken up into 4T1 cells, and the cellular uptake was increased steadily with the NSs concentration and the incubation time. For example, for a given incubation time of 6 h, the uptake by 4T1 cells incubated with 50 μg·mL^{-1} dispersion was ~ 1.84-fold as that incubated with the 20 μg·mL^{-1} dispersion (98.5 vs. 53.6 ng per 10^4 cells). For the 50 μg·mL^{-1} dispersion, the uptake at 6 h was ~ 73%; higher than that at 3 h (98.5 vs. 57.1 ng per 10^4 cells).

We then examined the cytotoxicity of the CoS-PEG NSs to 4T1 and HUVEC cells, using the standard CCK-8 assay. After treating with the CoS-PEG NSs dispersions at gradient concentrations (0–150 μg·mL^{-1}) for 24 h, the cell viability of both 4T1 cells and HUVEC cells remained over 80%, suggesting no significant cytotoxicity to either cells at the tested doses (Fig. 5(b)). Moreover, to further confirm their biocompatibility, we also investigated the influence of the CoS-PEG NSs on hemolysis of red blood cells (RBCs), using DI water and PBS as the positive and negative control groups. The hemolysis percentage was calculated via the following equation: Hemolysis percentage (%) = $(A_s - A_n)/(A_p - A_n) \times 100\%$, in which A_s, A_n, and A_p refer to the optical absorbance at 577 nm of the samples, the negative control, and the positive control, respectively. As shown in Fig. 5(c), negligible RBCs hemolysis behavior was observed and the calculated hemolysis percentage for a high concentration dispersion (200 μg·mL^{-1}) was less than 4%, clearly indicating the excellent blood compatibility of the CoS-PEG NSs. Therefore, these important results demonstrated that CoS-PEG NSs possess efficient cellular uptakes, no/low cytotoxicity, and good biocompatibility. All of these virtues ensure the favorable biosafety of the CoS-PEG NSs for cancer imaging and therapy.

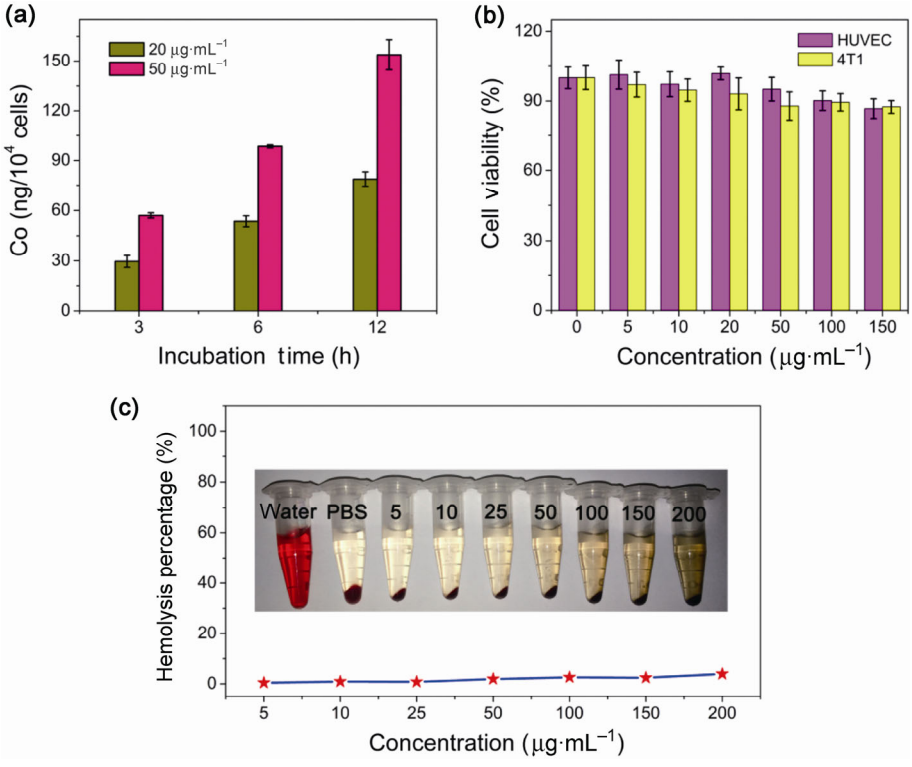

Figure 5 (a) Quantitative analysis (determined by ICP-MS) on cellular uptake of the CoS-PEG NSs by 4T1 cells vs. incubation time. (b) Cell viability of HUVEC and 4T1 cells after incubating with the CoS-PEG NSs suspension at gradient concentrations (0–150 μg·mL^{-1}) for 24 h. (c) Hemolysis percentage of RBCs after treating with the CoS-PEG NSs suspension at various concentrations for 4 h. Inset: The corresponding hemolytic photos taken from different groups.

3.4 IRT imaging and PTT effect on cancer cells

Before demonstrating the PTT efficacy on cancer cells, we first studied the *in vitro* IRT imaging performance on 4T1 cells (Fig. 6(a)). 4T1 cells were cultured separately in six wells (Nos. 1–6) on a 96-well plate, and then the CoS-PEG NSs dispersion was infused into wells Nos. 1, 2, 5, and 6, while a pure culture medium was added into the rest wells. The 808-nm irradiation (1.2 W·cm^{-2}, as indicated by a circle) was applied on wells Nos. 3, 4, 5, and 6. Before irradiation, all wells exhibited the same blue color relating to the initial room temperature. When the irradiation was applied, a high brightness representing the significant temperature elevation on the 4T1 cells was observed only from wells Nos. 5 and 6 in which the NSs participated. The imaging contrast, i.e. the thermal signal intensity, increased with the irradiation duration. Therefore, these results clearly demonstrate the excellent IRT imaging and temperature-elevation abilities of the Co-PEG NSs on 4T1 cells. Considering the high temperature reached upon the irradiation, the IRT images also suggest the pronounced PTT effect on killing cancer cells. We then performed the CCK-8 assay to evaluate the PTT efficacy of the CoS-PEG NSs by measuring the cell viability of 4T1 cells after treating with the NSs and laser irradiation. It was shown in Fig. 6(b) that the cell viability upon laser irradiation dramatically decreased as the NSs concentration increased from 0 to 60 μg·mL^{-1}, showing a prominent concentration-dependent photothermal killing effect. In particular, ~ 92% cells were destroyed after treated with 60 μg·mL^{-1} CoS-PEG NSs plus 10-min laser irradiation. In sharp contrast, the cell viability of the 4T1 cells was barely affected after only incubating with the CoS-PEG NSs dispersions without laser irradiation.

To intuitively display the PTT killing efficacy, 4T1 cells cultured in the 24-well plate were incubated with 60 μg·mL^{-1} CoS-PEG NSs dispersions, followed by exposure to the 808-nm laser for 10 min. After irradiation, a live-dead cell staining assay was carried out by co-staining 4T1 cells with calcein-AM (green fluorescence for living cells) and PI (red fluorescence for dead cells), followed by characterization using an inverted fluorescence microscope. As shown in Fig. 7, similar to the control group without any treatment, all of the 4T1 cells exhibited only vivid green and no red fluorescence signals after treating with either the CoS-PEG NSs or laser irradiation alone, indicating no obvious cell deaths induced by these two kinds of treatments. In contrast, the treatment combining the CoS-PEG NSs with laser irradiation caused a remarkable cell death accurately within the irradiation area (as marked by the yellow dashed line), directly revealing the effective NIR-mediated photothermal destruction of cancer cells. Therefore, our above results demonstrate great promise of the CoS-PEG NSs as an effective PTA for tumor PTT application.

3.5 PA and MR imaging

In addition to the significant IRT imaging and PTT

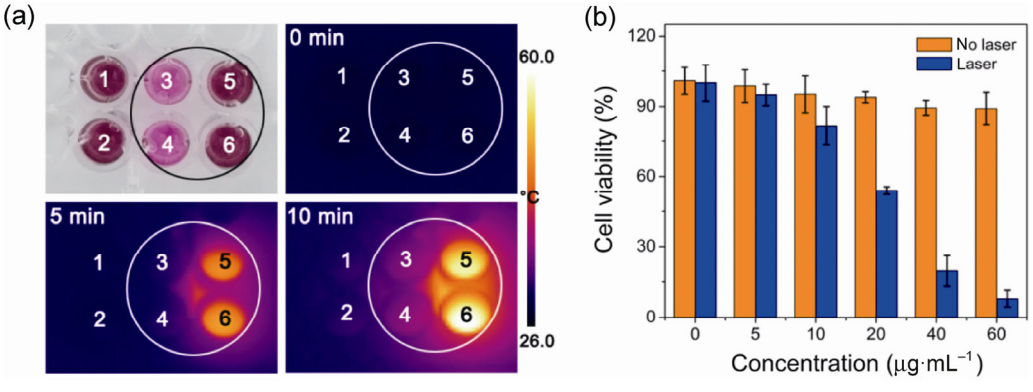

Figure 6 (a) *In vitro* IRT images of 4T1 cells treated with/without the CoS-PEG NSs and laser irradiation (marked by the circle), where well Nos. 1, 2, 5, and 6 contain both 4T1 cells and the CoS-PEG NSs suspension (60 μg·mL^{-1}), while well Nos. 3 and 4 only have 4T1 cells. (b) Cell viability of the 4T1 cells after treating with the CoS-PEG suspension at different concentrations (0–60 μg·mL^{-1}) upon 10-min of laser irradiation.

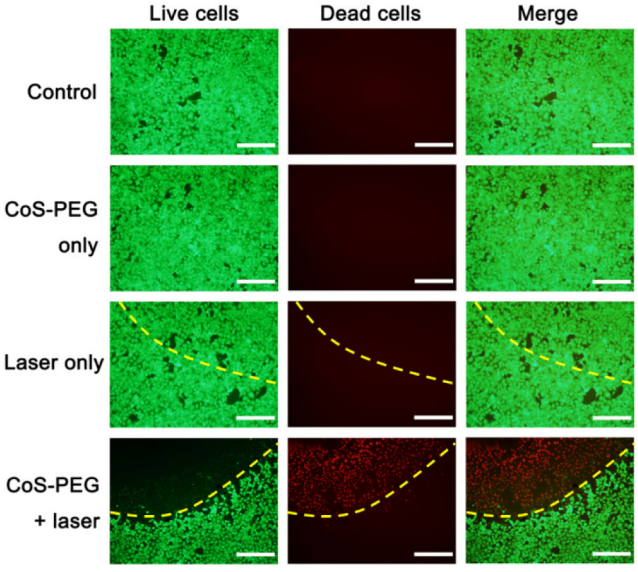

Figure 7 Fluorescence images of 4T1 cells stained with calcein-AM and PI after different treatments as indicated, i.e., blank control (untreated group); CoS-PEG only; laser only; and CoS-PEG + laser. The scale bar is 500 μm. The laser irradiation area is marked by the yellow dashed line.

therapeutic effects, the CoS-PEG NSs may also have potential for two other imaging modes, i.e., PA and MR imaging. PA imaging is a newly emerged hybrid imaging modality based on the PA effect and has received extensive attention in recent years because it combines the merits of acoustic and optical imaging, such as ultrahigh sensitivity, excellent spatial resolution, and deep tissue penetration depth [38]. Firstly, the PA imaging capability of the CoS-PEG NSs was investigated by scanning the PA images of the CoS-PEG NSs aqueous dispersions at gradient concentrations (0–320 μg·mL^{-1}). As shown in Fig. 8(a), the PA image of the NSs became brighter as the concentration increased gradually, suggesting incremental PA signals at a higher concentration.

The corresponding average PA signal intensity of each sample was then calculated (Fig. 8(b)), and a perfect linear relation of the PA intensity versus concentration was observed (R^2 = 0.996), indicating the outstanding PA imaging effects. To further investigate the *in vivo* PA imaging, a tumor-bearing mouse was i.t. injected with the CoS-PEG NSs dispersion and then anesthetized for PA scanning. As shown in Fig. 8(c), intense PA signals in the tumor area (indicated by the white circle) was observed after injection of the CoS-PEG NSs dispersion, in sharp contrast to that before the injection. On the other hand, due to the three unpaired electrons of Co [30], the CoS-PEG NSs can be promising candidates as T_2-weighted MRI contrast agents, capable of remedying the inherent limitations of PA imaging, such as the limited imaging penetration and high background interference [39], and provide a more comprehensive and powerful imaging function using the single nanoagent. We then assessed the MR imaging potential of the CoS-PEG NSs *in vitro* and *in vivo*. Firstly, the MR phantom imaging of the CoS-PEG NSs aqueous dispersions at gradient concentrations and the corresponding proton T_2 relaxation measurements were conducted under a 3.0 T MR clinical scanner. Encouragingly, much darker T_2-weighted MR images of the CoS-PEG NSs dispersions were observed, and the variation became more evident with increased NSs concentration, revealing a concentration-dependent MR enhancement effect (Fig. 8(d)). Moreover, as shown in Fig. 8(f), plots of the correlative proton transverse relaxation rate ($1/T_2$) versus NSs concentrations indicated a relatively good linear relation, confirming the promising negative enhancement for T_2 MR imaging. The T_2-MR enhancement effect on cancer cells was also studied by incubating 4T1 cells with the CoS-PEG NSs dispersions for MRI scanning. As anticipated, darker T_2 MRI images were observed in 4T1 cells treated with the CoS-PEG NSs than those without the NSs incubation (Fig. 8(e)), showing an efficient cellular uptake of the NSs for cancer cell MR imaging. For MR imaging of tumors *in vivo*, double-tumor-bearing mice were imaged under the 3.0 T MR scanning system after i.t. injecting the tumor on the right side with the CoS-PEG NSs, while the other tumor remained untreated as the control. The representative T_2-weighted MR transverse images of the mouse are shown in Fig. 8(g). The right tumor (No. 2) exhibited an obvious darkening effect, compared with the left tumor (No. 1) without NSs injection, indicating the prospective potency of the CoS-PEG NSs as a T_2-MRI agent *in vivo*. Thus, the presented results reveal that the CoS-PEG NSs could serve as a promising dual-modal imaging probe for simultaneous PA/MR imaging and may provide more valuable information for guiding PTT treatment.

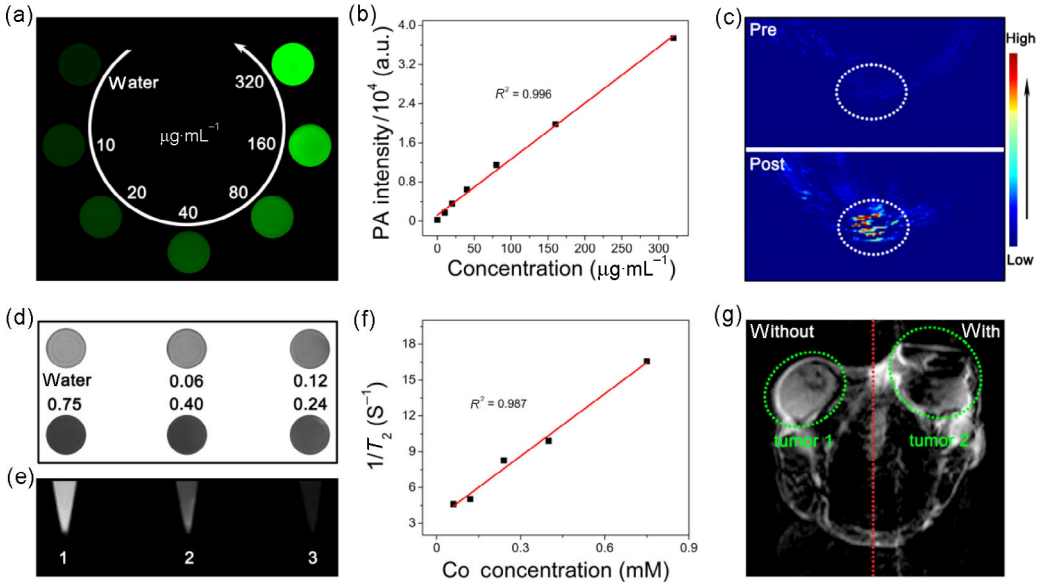

Figure 8 (a) *In vitro* PA images and (b) the corresponding PA intensity of the CoS-PEG aqueous dispersions at gradient concentrations as indicated. (c) Representative *in vivo* PA images of the tumor site before (Pre) and after (Post) injection with the CoS-PEG NSs dispersion. The tumor area is marked by the white dashed circle. (d) *In vitro* T_2-weighted MR images of the CoS-PEG NSs aqueous dispersions at gradient concentrations as indicated (unit: mmol·L^{-1}). (e) MR images of 4T1 cells (5×10^5 cells) dispersed in PBS (in 1.5 mL centrifuge tubes) after treating with the CoS-PEG NSs at different concentrations, where Nos. 1, 2, and 3 refer to the control group, and the NSs dispersion at 75 and 150 μg·mL^{-1}, respectively. (f) The analysis curve of the water proton transverse relaxation rate ($1/T_2$) versus Co concentration in the CoS-PEG dispersions. (g) Representative T_2-weighted MR transverse view of a double-tumor-bearing mouse, where Tumor 1 (located on the left side) without the NSs injection was used as the control, and Tumor 2 (on the right side) was injected with the CoS-PEG NSs dispersion. The tumor areas are marked by the green dashed circles.

4 Conclusions

In summary, we have successfully synthesized PEG-modified CoS-PEG NSs and unitized them as a versatile theranostic nanoplatform for multimodal imaging and photothermal ablation of cancer cells for the first time in the literature. The obtained CoS-PEG NSs possesses high compatibility and stability in water as well as in various physiological solutions. Excitingly, we demonstrated that the CoS-PEG NSs can be effectively internalized by cancer cells but show low cytotoxicity. Importantly, the CoS-PEG NSs exhibit strong NIR absorption, high photothermal conversion efficiency (~ 33.0%) and excellent photothermal stability. Moreover, we have demonstrated that the NSs can induce a significant photothermal ablation effect on cancer cells upon NIR laser irradiation, and the PTT effect follows a concentration-dependent manner. In addition, benefiting from the strong NIR absorbance as well as the T_2-MR contrasting ability of the CoS-PEG NSs, high-contrast PA, IRT, and MR imaging has been achieved, showing great potential for multimodal imaging to provide comprehensive cancer diagnoses. Moreover, thanks to the high specific surface area of the nanosheets, the CoS-PEG NSs may also hold great potential for drug loading. In addition, it has been demonstrated that nanoparticles smaller than ~ 400 nm could passively accumulate in the tumor via the enhanced permeability and retention (EPR) effect [40], and nanoparticles larger than ~ 50 nm could be cleared partially through the hepatobiliary pathway [41, 42]. Although the size of the CoS-PEG NSs (~ 179 nm) may have provided the EPR effect and clearance capability, a detailed *in vivo* study would be helpful to understand their possible physiological degradation mechanisms in the complex physiological environment. Further studies on targeted cancer therapy via conjugation of targeting ligands, loading drugs for combined therapies, *in vivo* distribution, and long-term toxicity are underway. The study presented shows great promise for CoS-PEG NSs as

biocompatible and powerful theranostic nanoplatforms for triple-modal imaging and PTT applications.

Acknowledgements

This work was financially supported by the National Natural Science Foundation of China (NSFC) (Nos. 21473045 and 51401066), the Fundamental Research Funds from the Central University (PIRSOF HIT A201503), and the State Key Laboratory of Urban Water Resource and Environment, the Harbin Institute of Technology (No. 2018DX04).

Electronic Supplementary Material: Supplementary material is available in the online version of this article at https://doi.org/10.1007/s12274-017-1865-z.

References

[1] Ou, G.; Li, Z. W.; Li, D. K.; Cheng, L.; Liu, Z.; Wu, H. Photothermal therapy by using titanium oxide nanoparticles. *Nano Res.* **2016**, *9*, 1236–1243.

[2] Siegel, R.; Naishadham, D.; Jemal, A. Cancer statistics, 2013. *CA-Cancer J. Clin.* **2013**, *63*, 11–30.

[3] Zhu, C. Q.; Yang, Y. H.; Luo, M.; Yang, C. X.; Wu, J. J.; Chen, L. N.; Liu, G.; Wen, T. B.; Zhu, J.; Xia, H. P. Stabilizing two classical antiaromatic frameworks: Demonstration of photoacoustic imaging and the photothermal effect in metalla-aromatics. *Angew. Chem., Int. Ed.* **2015**, *127*, 6279–6283.

[4] Yang, K.; Hu, L. L.; Ma, X. X.; Ye, S. Q.; Cheng, L.; Shi, X. Z.; Li, C. H.; Li, Y. G.; Liu, Z. Multimodal imaging guided photothermal therapy using functionalized graphene nanosheets anchored with magnetic nanoparticles. *Adv. Mater.* **2012**, *24*, 1868–1872.

[5] Shao, J. D.; Xie, H. H.; Huang, H.; Li, Z. B.; Sun, Z. B.; Xu, Y. H.; Xiao, Q. L.; Yu, X. F.; Zhao, Y. T.; Zhang, H. et al. Biodegradable black phosphorus-based nanospheres for *in vivo* photothermal cancer therapy. *Nat. Commun.* **2016**, *7*, 12967.

[6] Zhao, Z. X.; Shi, S. G.; Huang, Y. H.; Tang, S. H.; Chen, X. L. Simultaneous photodynamic and photothermal therapy using photosensitizer-functionalized Pd nanosheets by single continuous wave laser. *ACS Appl. Mater. Interfaces* **2014**, *6*, 8878–8885.

[7] Zhang, Z. J.; Wang, L. M.; Wang, J.; Jiang, X. M.; Li, X. H.; Hu, Z. J.; Ji, Y. L.; Wu, X. C.; Chen, C. Y. Mesoporous silica-coated gold nanorods as a light-mediated multifunctional theranostic platform for cancer treatment. *Adv. Mater.* **2012**, *24*, 1418–1423.

[8] Huang, X. Q.; Tang, S. H.; Mu, X. L.; Dai, Y.; Chen, G. X.; Zhou, Z. Y.; Ruan, F. X.; Yang, Z. L.; Zheng, N. F. Freestanding palladium nanosheets with plasmonic and catalytic properties. *Nat. Nanotechnol.* **2011**, *6*, 28–32.

[9] Yang, K.; Zhang, S.; Zhang, G. X.; Sun, X. M.; Lee, S. T.; Liu, Z. Graphene in mice: Ultrahigh *in vivo* tumor uptake and efficient photothermal therapy. *Nano Lett.* **2010**, *10*, 3318–3323.

[10] Cheng, L.; Liu, J. J.; Gu, X.; Gong, H.; Shi, X. Z.; Liu, T.; Wang, C.; Wang, X. Y.; Liu, G.; Xing, H. Y. et al. PEGylated WS_2 nanosheets as a multifunctional theranostic agent for *in vivo* dual-modal CT/photoacoustic imaging guided photothermal therapy. *Adv. Mater.* **2014**, *26*, 1886–1893.

[11] Chou, S. S.; Kaehr, B.; Kim, J.; Foley, B. M.; De, M.; Hopkins, P. E.; Huang, J. X.; Brinker, C. J.; Dravid, V. P. Chemically exfoliated MoS_2 as near-infrared photothermal agents. *Angew. Chem., Int. Ed.* **2013**, *125*, 4254–4258.

[12] Li, Z. L.; Liu, J.; Hu, Y.; Howard, K. A.; Li, Z.; Fan, X. L.; Chang, M. L.; Sun, Y.; Besenbacher, F.; Chen, C. Y. et al. Multimodal imaging-guided antitumor photothermal therapy and drug delivery using bismuth selenide spherical sponge. *ACS Nano* **2016**, *10*, 9646–9658.

[13] Li, Z. L.; Hu, Y.; Chang, M. L.; Howard, K. A.; Fan, X. L.; Sun, Y.; Besenbacher, F.; Yu, M. Highly porous PEGylated Bi_2S_3 nano-urchins as a versatile platform for *in vivo* triple-modal imaging, photothermal therapy and drug delivery. *Nanoscale* **2016**, *8*, 16005–16016.

[14] Li, Z. L.; Hu, Y.; Howard, K. A.; Jiang, T. T.; Fan, X. L.; Miao, Z. H.; Sun, Y.; Besenbacher, F.; Yu, M. Multifunctional bismuth selenide nanocomposites for antitumor thermo-chemotherapy and imaging. *ACS Nano* **2016**, *10*, 984–997.

[15] Zhang, C.; Fu, Y. Y.; Zhang, X. J.; Yu, C. S.; Zhao, Y.; Sun, S. K. BSA-directed synthesis of CuS nanoparticles as a biocompatible photothermal agent for tumor ablation *in vivo*. *Dalton T.* **2015**, *44*, 13112–13118.

[16] Yang, T.; Wang, Y.; Ke, H. T.; Wang, Q. L.; Lv, X. Y.; Wu, H.; Tang, Y. A.; Yang, X. L.; Chen, C. Y.; Zhao, Y. L. et al. Protein-nanoreactor-assisted synthesis of semiconductor nanocrystals for efficient cancer theranostics. *Adv. Mater.* **2016**, *28*, 5923–5930.

[17] Chen, W. S.; Ouyang, J.; Liu, H.; Chen, M.; Zeng, K.; Sheng, J. P.; Liu, Z. J.; Han, Y. J.; Wang, L. Q.; Li, J. et al. Black phosphorus nanosheet-based drug delivery system for synergistic photodynamic/photothermal/chemotherapy of cancer. *Adv. Mater.* **2017**, *29*, 1603864.

[18] Lovell, J. F.; Jin, C. S.; Huynh, E.; Jin, H.; Kim, C.; Rubinstein, J. L.; Chan, W. C.; Cao, W. G.; Wang, L. V.; Zheng, G. Porphysome nanovesicles generated by porphyrin bilayers for use as multimodal biophotonic contrast agents.

Nat. Mater. **2011**, *10*, 324–332.

[19] Janib, S. M.; Moses, A. S.; MacKay, J. A. Imaging and drug delivery using theranostic nanoparticles. *Adv. Drug Deliver. Rev.* **2010**, *62*, 1052–1063.

[20] Yang, K.; Yang, G. B. ; Chen, L.; Cheng, L.; Wang, L.; Ge, C. C.; Liu, Z. FeS nanoplates as a multifunctional nano-theranostic for magnetic resonance imaging guided photothermal therapy. *Biomaterials* **2015**, *38*, 1–9.

[21] Zhang, Z. J.; Wang, J.; Chen, C. Y. Near-infrared light-mediated nanoplatforms for cancer thermo-chemotherapy and optical imaging. *Adv. Mater.* **2013**, *25*, 3869–3880.

[22] Wang, L. R.; Zhu, X. L.; Tang, X. Y.; Wu, C. Q.; Zhou, Z. J.; Sun, C. J.; Deng, S. L.; Ai, H.; Gao, J. H. A multiple gadolinium complex decorated fullerene as a highly sensitive T_1 contrast agent. *Chem. Commun.* **2015**, *51*, 4390–4393.

[23] Rieke, V.; Butts Pauly, K. MR thermometry. *J. Magn. Reson. Imaging* **2008**, *27*, 376–390.

[24] Tian, Q. W.; Hu, J. Q.; Zhu, Y. H.; Zou, R. J.; Chen, Z. G.; Yang, S. P.; Li, R. W.; Su, Q. Q.; Han, Y.; Liu, X. G. Sub-10 nm Fe_3O_4@$Cu_{2-x}S$ core-shell nanoparticles for dual-modal imaging and photothermal therapy. *J. Am. Chem. Soc.* **2013**, *135*, 8571–8577.

[25] Fu, G. L.; Liu, W.; Li, Y. Y.; Jin, Y. S.; Jiang, L. D.; Liang, X. L.; Feng, S. S.; Dai, Z. F. Magnetic prussian blue nanoparticles for targeted photothermal therapy under magnetic resonance imaging guidance. *Bioconjugate Chem.* **2014**, *25*, 1655–1663.

[26] Song, G. S.; Liang, C.; Gong, H.; Li, M. F.; Zheng, X. C.; Cheng, L.; Yang, K.; Jiang, X. Q.; Liu, Z. Core-shell MnSe@Bi_2Se_3 fabricated via a cation exchange method as novel nanotheranostics for multimodal imaging and synergistic thermoradiotherapy. *Adv. Mater.* **2015**, *27*, 6110–6117.

[27] Song, X. R.; Wang, X. Y.; Yu, S. X.; Cao, J. B.; Li, S. H.; Li, J.; Liu, G.; Yang, H. H.; Chen, X. Y. Co_9Se_8 nanoplates as a new theranostic platform for photoacoustic/magnetic resonance dual-modal-imaging-guided chemo-photothermal combination therapy. *Adv. Mater.* **2015**, *27*, 3285–3291.

[28] Xie, J.; Lee, S.; Chen, X. Y. Nanoparticle-based theranostic agents. *Adv. Drug Deliver. Rev.* **2010**, *62*, 1064–1079.

[29] Menon, J. U.; Jadeja, P.; Tambe, P.; Vu, K.; Yuan, B. H.; Nguyen, K. T. Nanomaterials for photo-based diagnostic and therapeutic applications. *Theranostics* **2013**, *3*, 152–166.

[30] Parkes, L. M.; Hodgson, R.; Lu, L. T.; Tung, L. D.; Robinson, I.; Fernig, D. G.; Thanh, N. T. K. Cobalt nanoparticles as a novel magnetic resonance contrast agent-relaxivities at 1.5 and 3 Tesla. *Contrast Media Mol. I.* **2008**, *3*, 150–156.

[31] Li, B.; Yuan, F. K.; He, G. J.; Han, X. Y.; Wang, X.; Qin, J. B.; Guo, Z. X.; Lu, X. W.; Wang, Q.; Parkin, I. P. et al. Ultrasmall $CuCo_2S_4$ nanocrystals: All-in-one theragnosis nanoplatform with magnetic resonance/near-infrared imaging for efficiently photothermal therapy of tumors. *Adv. Funct. Mater.* **2017**, *27*, 1606218.

[32] Huang, X. J.; Deng, G. Y.; Liao, L. J.; Zhang, W. L.; Guan, G. Q.; Zhou, F.; Xiao, Z. Y.; Zou, R. J.; Wang, Q.; Hu, J. Q. $CuCo_2S_4$ nanocrystals: A new platform for multimodal imaging guided photothermal therapy. *Nanoscale* **2017**, *9*, 2626–2632.

[33] Yang, Z. S.; Chen, C. Y.; Chang, H. T. Supercapacitors incorporating hollow cobalt sulfide hexagonal nanosheets. *J. Power Sources* **2011**, *196*, 7874–7877.

[34] Sun, L.; Lin, Z.; Peng, J.; Weng, J.; Huang, Y.; Luo, Z. Preparation of few-layer bismuth selenide by liquid-phase-exfoliation and its optical absorption properties. *Sci. Rep.* **2014**, *4*, 4794.

[35] Li, Z. L.; Zeng, Y. Y.; Zhang, D.; Wu, M.; Wu, L. J.; Huang, A. M.; Yang, H. H.; Liu, X. L.; Liu, J. F. Glypican-3 antibody functionalized prussian blue nanoparticles for targeted MR imaging and photothermal therapy of hepatocellular carcinoma. *J. Mater. Chem. B* **2014**, *2*, 3686–3696.

[36] Roper, D. K.; Ahn, W.; Hoepfner, M. Microscale heat transfer transduced by surface plasmon resonant gold nano-particles. *J. Phys. Chem. C* **2007**, *111*, 3636–3641.

[37] Hessel, C. M.; Pattani, V. P.; Rasch, M.; Panthani, M. G.; Koo, B.; Tunnell, J. W.; Korgel, B. A. Copper selenide nanocrystals for photothermal therapy. *Nano Lett.* **2011**, *11*, 2560–2566.

[38] Wang, L. V.; Hu, S. Photoacoustic tomography: *In vivo* imaging from organelles to organs. *Science* **2012**, *335*, 1458–1462.

[39] Chen, J. Q.; Liu, C. B.; Hu, D. H.; Wang, F.; Wu, H. W.; Gong, X. J.; Liu, X.; Song, L.; Sheng, Z. H.; Zheng, H. R. Single-layer MoS_2 nanosheets with amplified photoacoustic effect for highly sensitive photoacoustic imaging of orthotopic brain tumors. *Adv. Funct. Mater.* **2016**, *26*, 8715–8725.

[40] Wang, X. G.; Dong, Z. Y.; Cheng, H.; Wan, S. S.; Chen, W. H.; Zou, M. Z.; Huo, J. W.; Deng, H. X.; Zhang, X. Z. A multifunctional metal-organic framework based tumor targeting drug delivery system for cancer therapy. *Nanoscale* **2015**, *7*, 16061–16070.

[41] Zhang, X. D.; Chen, J.; Min, Y.; Park, G. B.; Shen, X.; Song, S. S.; Sun, Y. M.; Wang, H.; Long, W.; Xie, J. P. et al. Metabolizable Bi_2Se_3 nanoplates: Biodistribution, toxicity, and uses for cancer radiation therapy and imaging. *Adv. Funct. Mater.* **2014**, *24*, 1718–1729.

[42] Zhang, X. D.; Luo, Z. T.; Chen, J.; Shen, X.; Song, S. S.; Sun, Y. M.; Fan, S. J.; Fan, F. Y.; Leong, D. T.; Xie, J. P. Ultrasmall $Au_{10-12}(SG)_{10-12}$ nanomolecules for high tumor specificity and cancer radiotherapy. *Adv. Mater.* **2014**, *26*, 4565–4568.